Auxiliary figures for

Subduction Initiation from a Stagnant Lid and Global Overturn: New Insights from Numerical Models with a Free Surface

Fabio Crameri[1,2,3] and Paul J. Tackley[3]

[1]Centre for Earth Evolution and Dynamics, University of Oslo, Postbox 1028 Blindern, 0315 Oslo, Norway.
[2]Department of Earth Sciences, University College London, Gower Street, London WC1E 6BT, United Kingdom.
[3]Department of Earth Sciences, ETH Zurich, Sonneggstrasse 5, 8092 Zurich, Switzerland.

Progress in Earth and Planetary Science, 2016

Contents

S1 Supplementary Figures: Regional Model

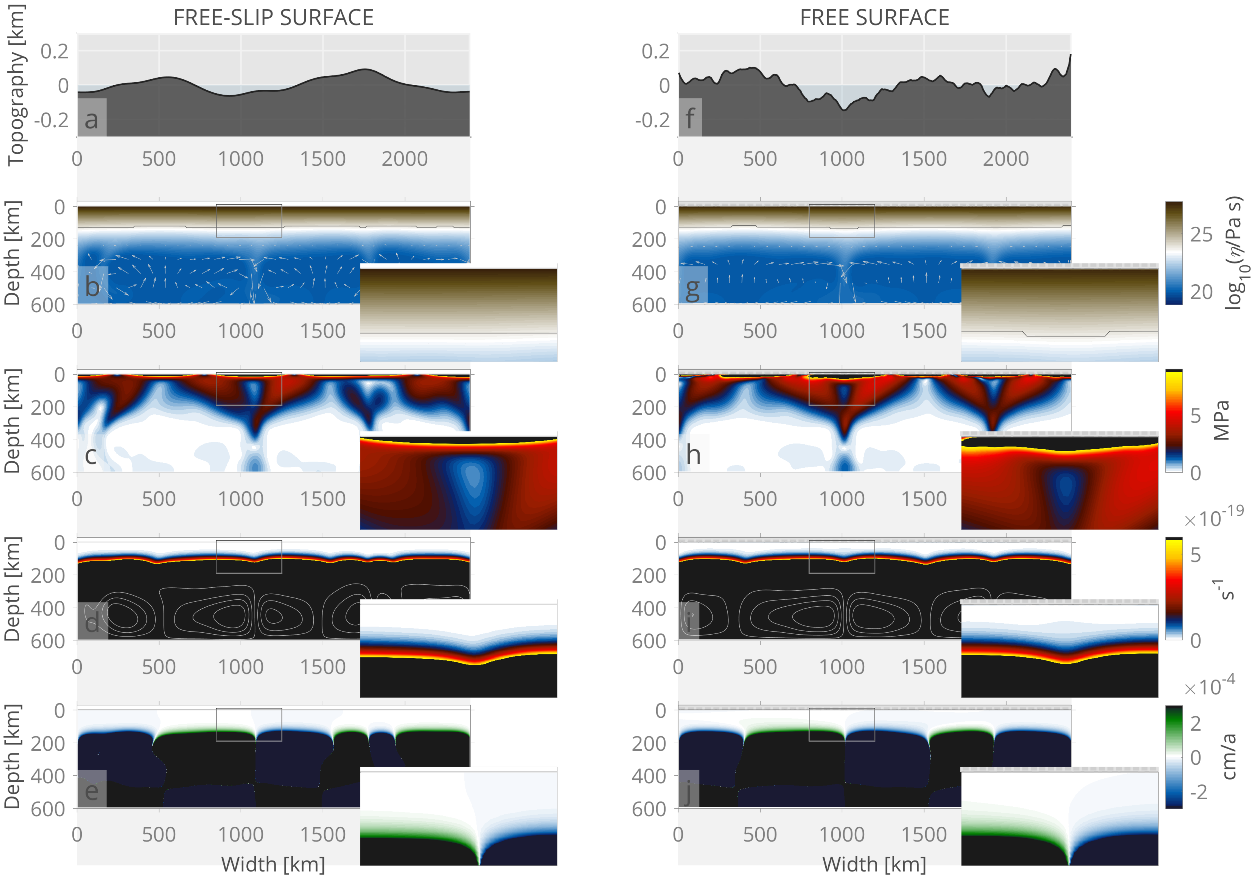

Figure S1.1: **Free-slip versus free surface steady-state stagnant-lid with no yielding.** Small-scale convection experiments *lid*01 with a free-slip surface (left hand side column) and *lid*02 with a free surface (right hand side column) both without plastic yielding. (a) Surface topography of the free-slip top boundary model that is calculated from the normal stress occurring at the vertically-fixed, top domain boundary and (f) the actual topography that occurs in the model with the free top boundary. (b,g) Effective viscosity and the 700 K contour (black line), (c,h) second invariant of the strain rate, (d,i) second invariant of stress, and (e,j) horizontal velocity are shown for both models, where green colours indicate flow in clockwise direction. Very high values are clipped in regions where they exceed a certain maximum value (black areas). White arrows and grey streamlines indicate the flow direction.

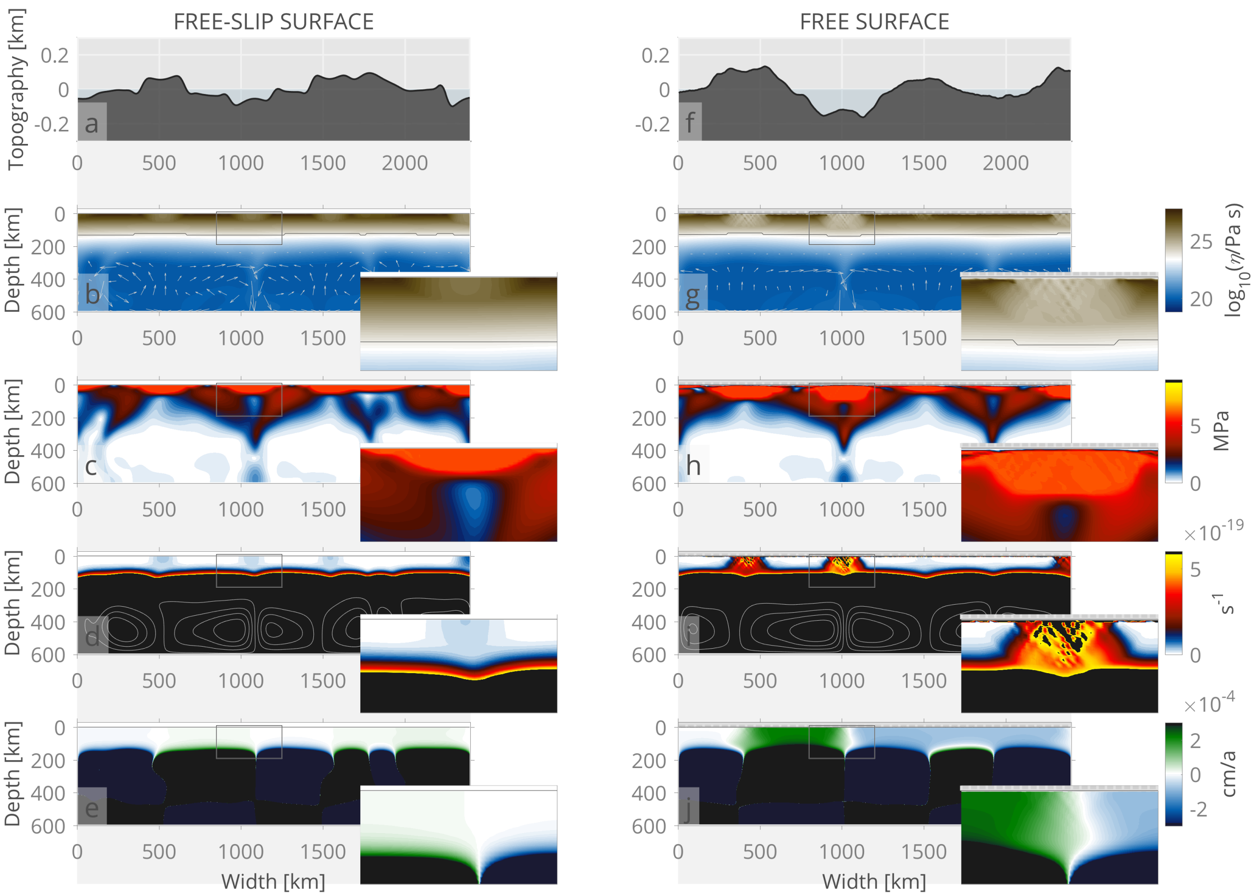

Figure S1.2: **Free-slip versus free surface steady-state stagnant-lid with depth-constant yielding.** Small-scale convection experiments *lidA*2 with a free-slip surface (left hand side column) and *lidA*5 with a free surface (right hand side column) both with a maximum, depth-constant yield stress. (a) Surface topography of the free-slip top boundary model that is calculated from the normal stress occurring at the vertically-fixed, top domain boundary and (f) the actual topography that occurs in the model with the free top boundary. (b,g) Effective viscosity and the 700 K contour (black line), (c,h) second invariant of the strain rate, (d,i) second invariant of stress, and (e,j) horizontal velocity are shown for both models, where green colours indicate flow in clockwise direction. Very high values are clipped in regions where they exceed a certain maximum value (black areas). White arrows and grey streamlines indicate the flow direction.

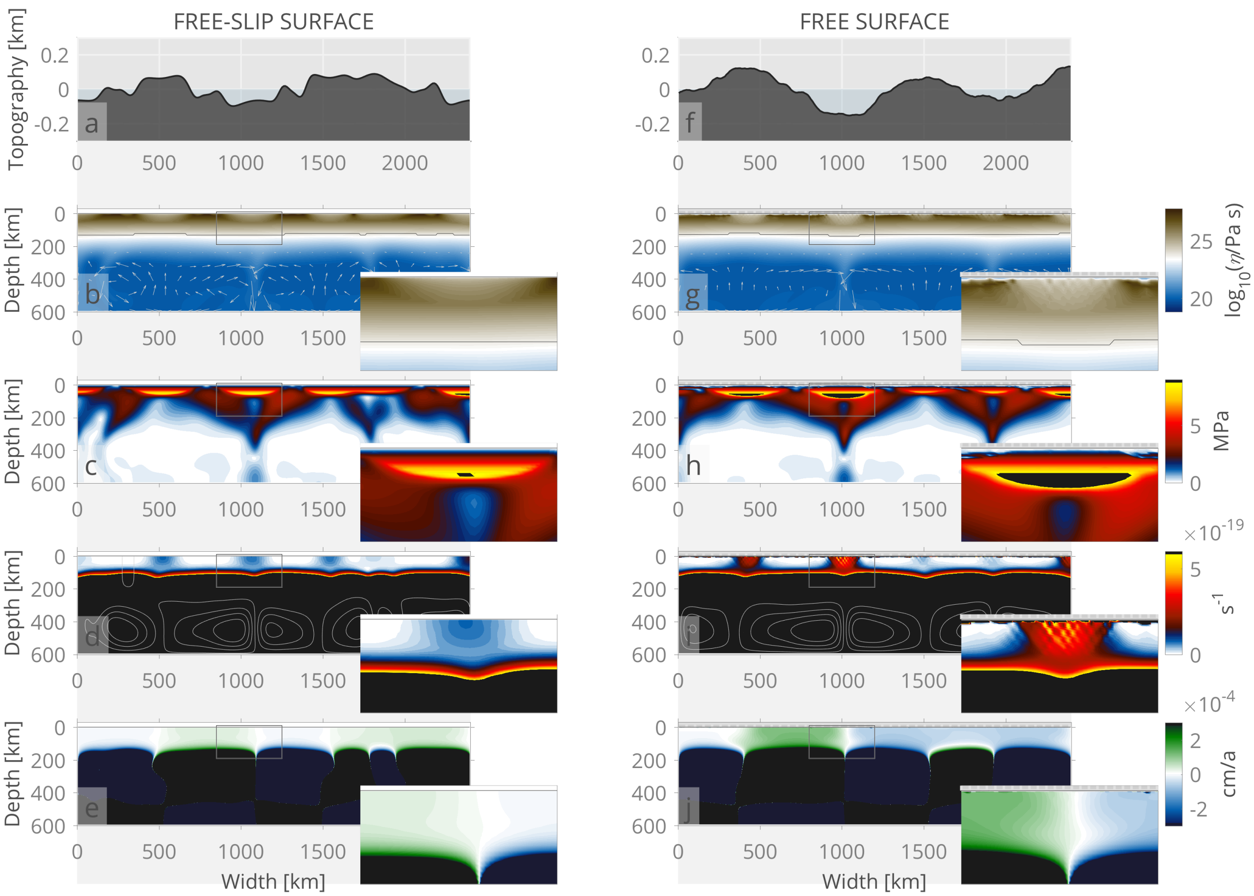

Figure S1.3: **Free-slip versus free surface steady-state stagnant-lid with depth-dependent yielding.** Small-scale convection experiments *lidB*3 with a free-slip surface (left hand side column) and *lidB*7 with a free surface (right hand side column) both with a depth-dependent yield stress. (a) Surface topography of the free-slip top boundary model that is calculated from the normal stress occurring at the vertically-fixed, top domain boundary and (f) the actual topography that occurs in the model with the free top boundary. (b,g) Effective viscosity and the 700 K contour (black line), (c,h) second invariant of the strain rate, (d,i) second invariant of stress, and (e,j) horizontal velocity are shown for both models, where green colours indicate flow in clockwise direction. Very high values are clipped in regions where they exceed a certain maximum value (black areas). White arrows and grey streamlines indicate the flow direction.

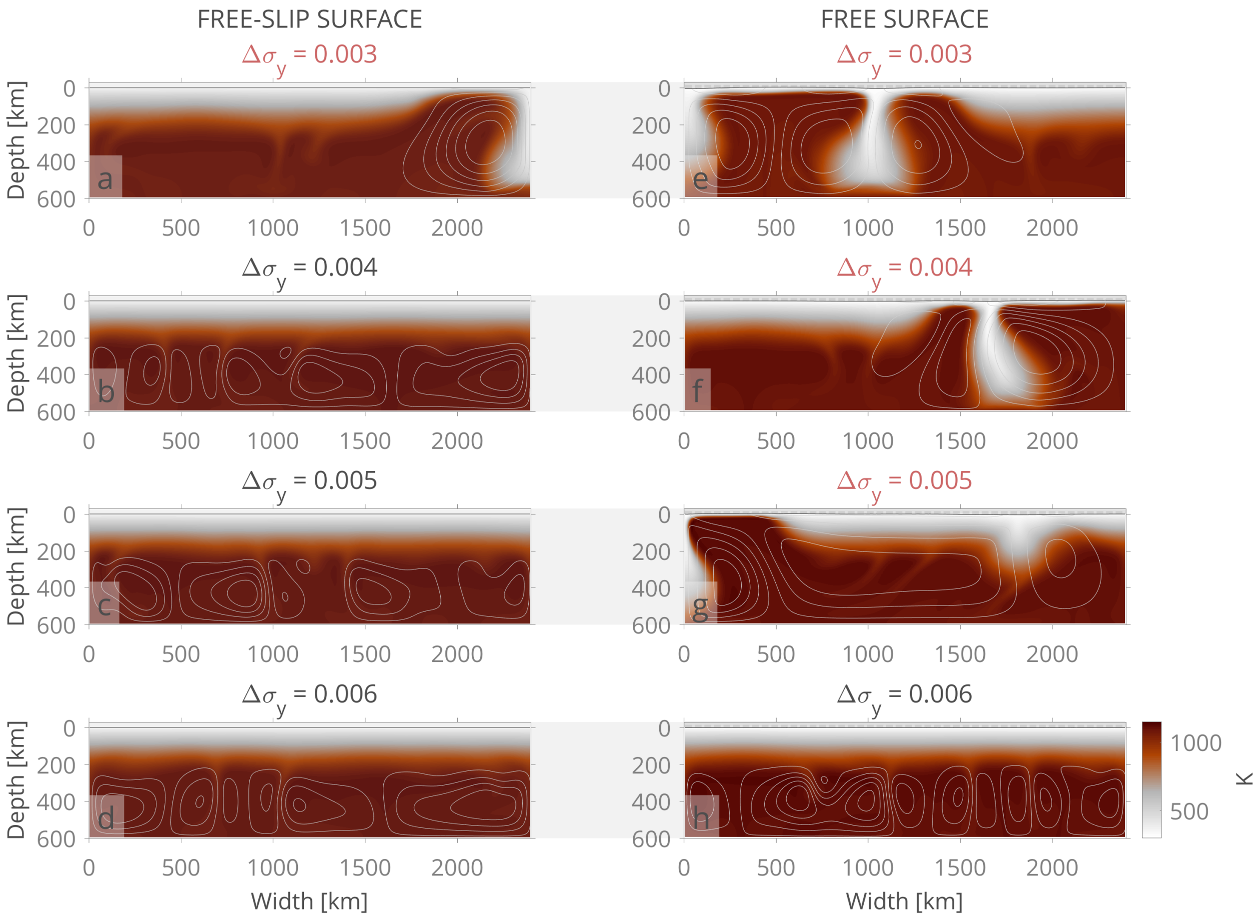

Figure S1.4: **Occurrence of SI with variable depth-dependent yield stress.** Subduction initiation by small-scale convection (after Solomatov, 2004) depending on the depth-dependent yield stress $\Delta\sigma_y$ that varies from the non-dimensional value of (a,e) $\Delta\sigma_y = 0.003$ ($lidB1$ & $lidB5$) to (d,h) $\Delta\sigma_y = 0.006$ ($lidB4$ & $lidB8$). The temperature fields are shown for experiments employing a free-slip surface (left hand side column) and a free surface (right hand side column). Grey contours indicate streamlines of the flow and the red title colour indicates onset of subduction.

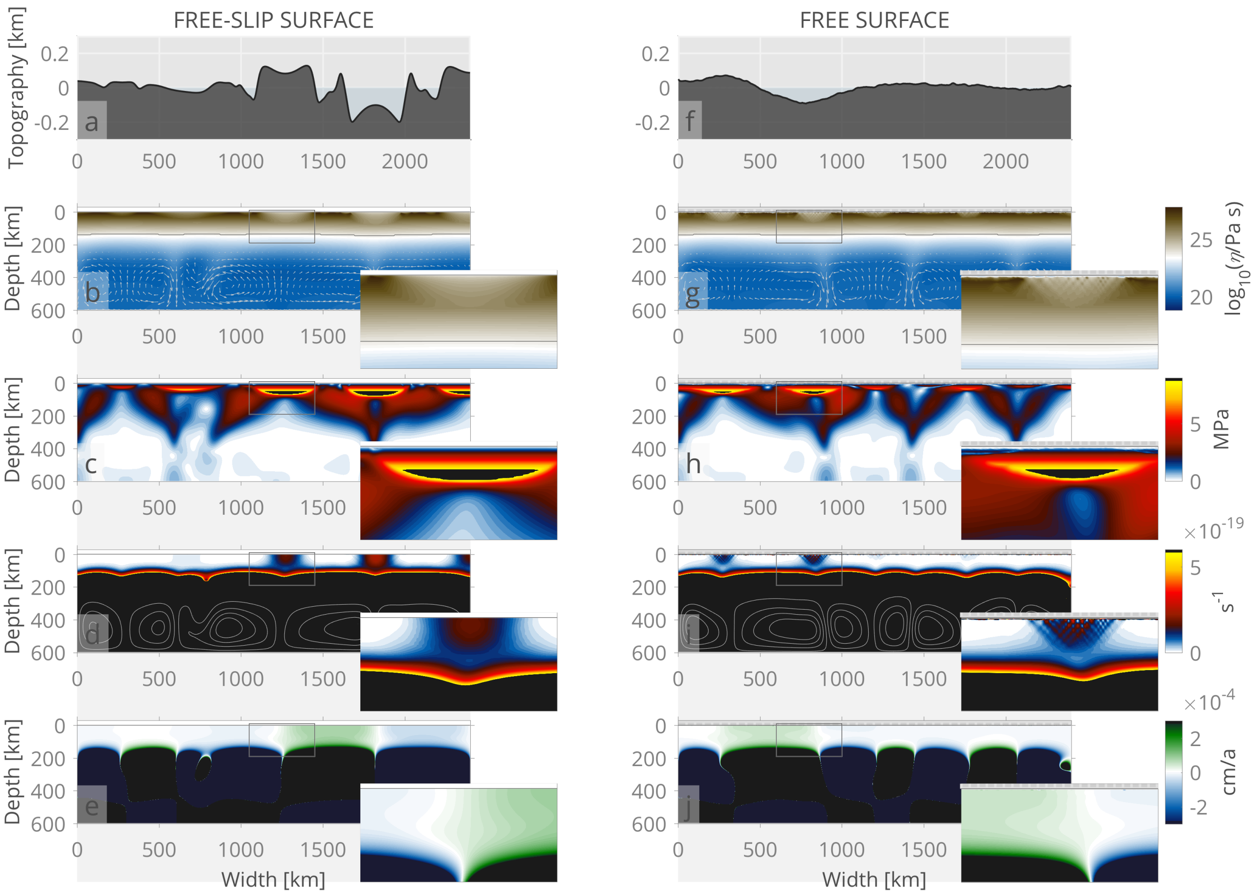

Figure S1.5: **Double resolution test for composite yield stress model.** Two times standard resolution, small-scale convection experiments $lidC2_{highres2}$ with a free-slip surface (left hand side column) and $lidC5_{highres2}$ with a free surface (right hand side column) both employing a composite yield stress with a yield stress gradient of $\Delta\sigma_y = 0.0054$ and a dimensional, constant yield stress of $\sigma_{y,const} = 8.7$ MPa. (a) Surface topography of the free-slip top boundary model that is calculated from the normal stress occurring at the vertically-fixed, top domain boundary and (f) the actual topography that occurs in the model with the free top boundary. (b,g) Effective viscosity and the 700 K contour (black line), (c,h) second invariant of the strain rate, (d,i) second invariant of stress, and (e,j) horizontal velocity are shown for both models, where green colours indicate flow in clockwise direction. If applied, the sticky-air layer is removed visually and replaced with a hatched grey area. Very high values are clipped in regions where they exceed a certain maximum value (black areas). White arrows and grey streamlines indicate the flow direction and pattern.

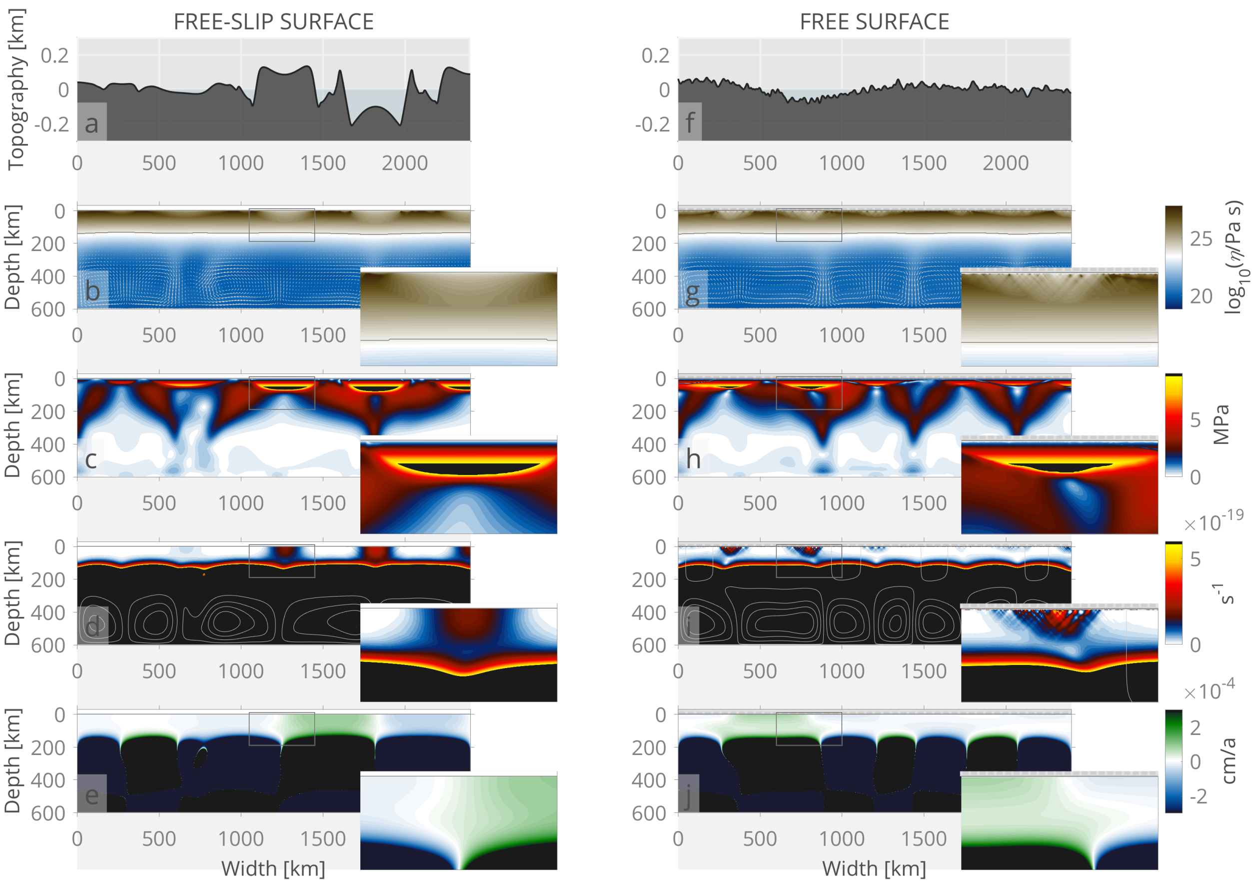

Figure S1.6: **Quadruple resolution test for composite yield stress model.** Four times standard resolution, small-scale convection experiments $lidC2_{highres4}$ with a free-slip surface (left hand side column) and $lidC5_{highres4}$ with a free surface (right hand side column) both employing a composite yield stress with a yield stress gradient of $\Delta\sigma_y = 0.0054$ and a dimensional, constant yield stress of $\sigma_{y,const} = 8.7$ MPa. (a) Surface topography of the free-slip top boundary model that is calculated from the normal stress occurring at the vertically-fixed, top domain boundary and (f) the actual topography that occurs in the model with the free top boundary. (b,g) Effective viscosity and the 700 K contour (black line), (c,h) second invariant of the strain rate, (d,i) second invariant of stress, and (e,j) horizontal velocity are shown for both models, where green colours indicate flow in clockwise direction. If applied, the sticky-air layer is removed visually and replaced with a hatched grey area. Very high values are clipped in regions where they exceed a certain maximum value (black areas). White arrows and grey streamlines indicate the flow direction and pattern.

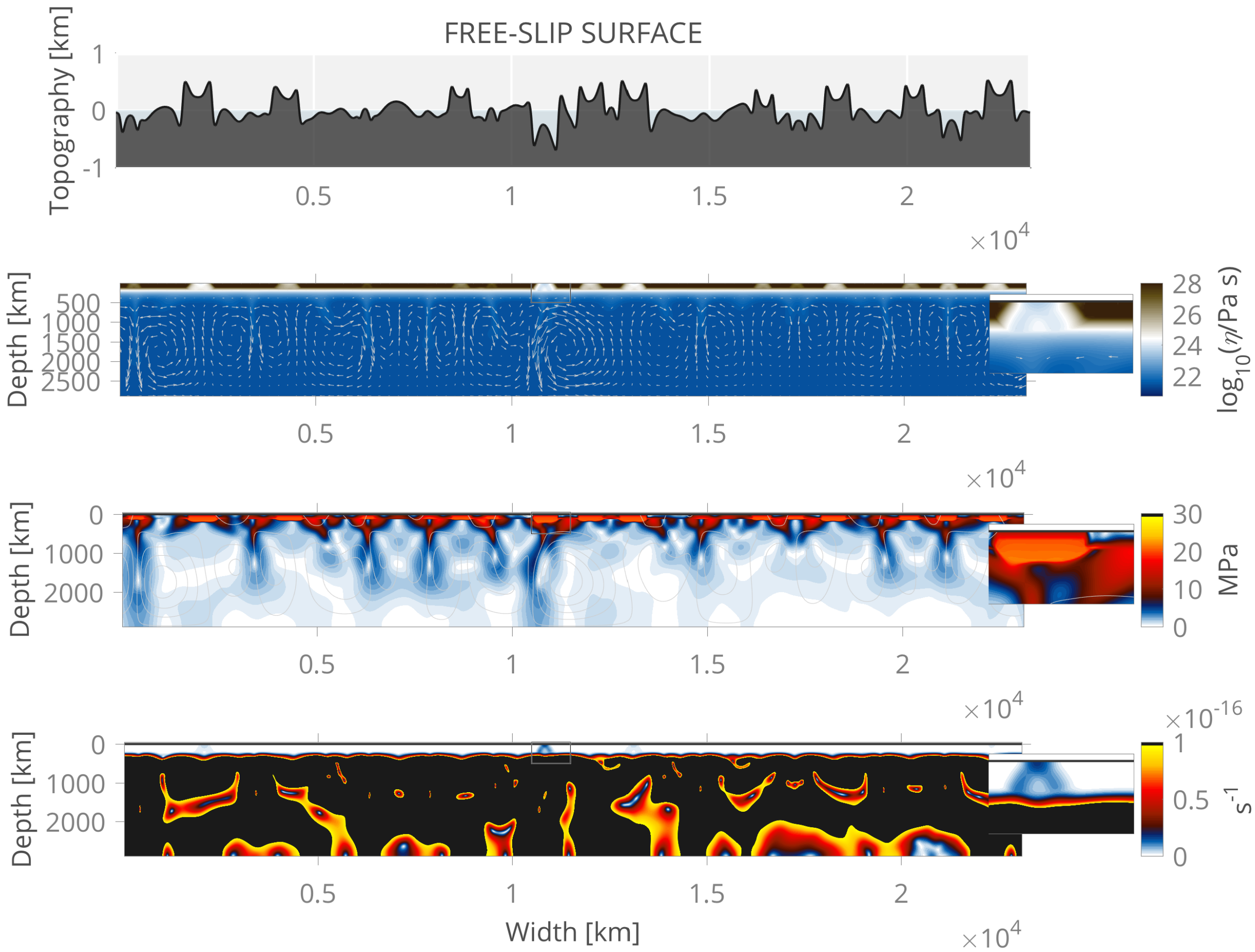

Figure S1.7: **Free-slip surface steady-state stagnant-lid in the 2-D global models.** Lithosphere-scale yielding induced by global-scale convection of experiment *global*1 with a free-slip surface. The model employs a composite yield stress with a yield stress gradient of $\Delta\sigma_y = 0.005$ and a dimensional, constant yield stress of $\sigma_{y,const} = 21.7$ MPa. Shown are (a) surface topography of the free-slip top boundary model that is calculated from the normal stress occurring at the vertically-fixed, top domain boundary, (b) effective viscosity, (c) second invariant of the strain rate, and (d) second invariant of stress. Very high values are clipped in regions where they exceed a certain maximum value (black areas). White arrows and grey streamlines indicate the flow direction and pattern.

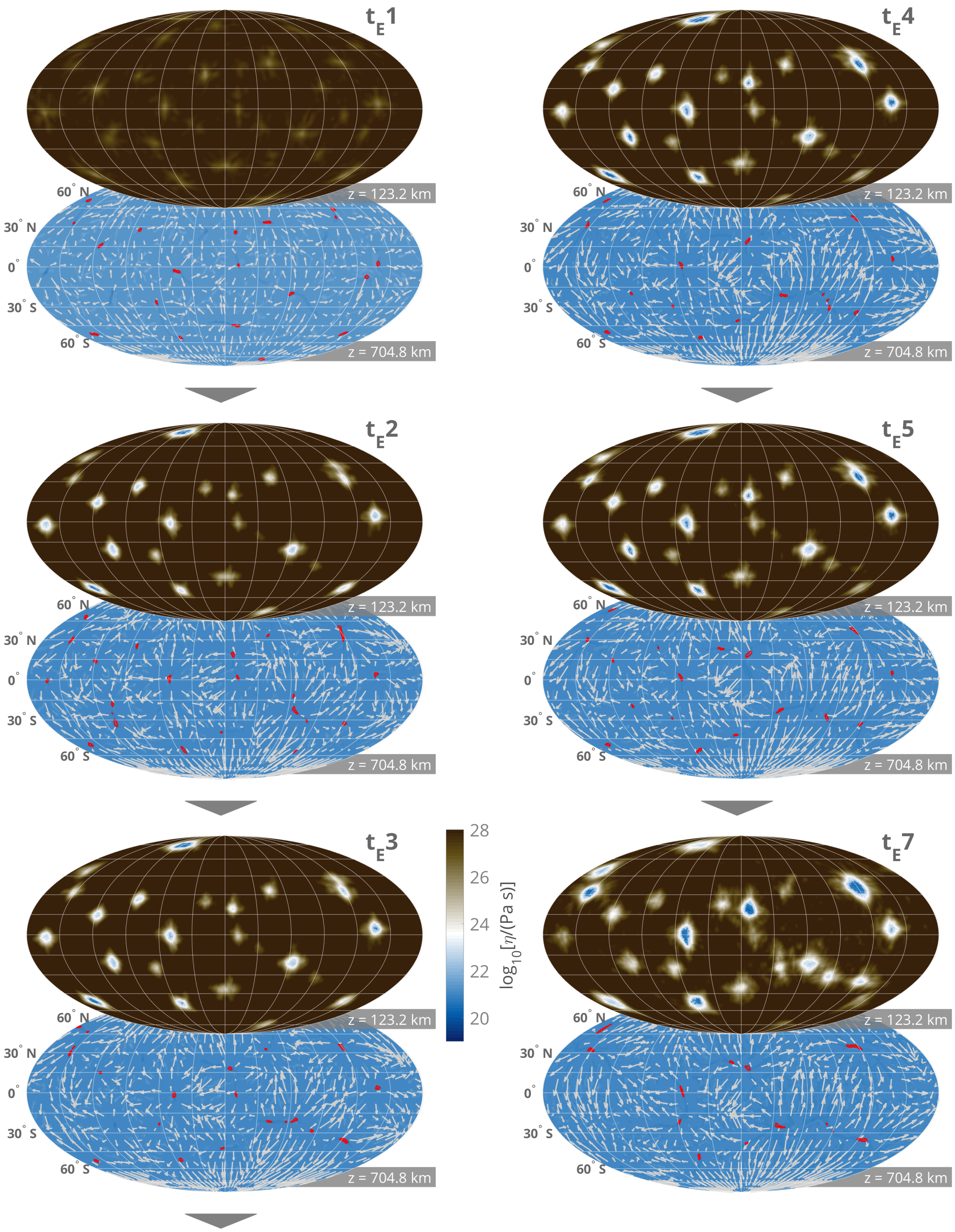

Figure S1.8: **Stagnant-lid convection in 3-D fully spherical model with a free-slip surface.** Temporal evolution of an internally and basally heated, global spherical experiment (*global*3) starting from an initial stagnant lid (without initial subduction zone) shown by horizontal slides at 123 km (top subplot) and 704 km (bottom subplot) depth. Anomalously hot ($f_{hot} = 0.45$) regions compared to the horizontal mean temperature that are connected to the CMB are extracted by the plume tracking software and indicated by a red contour. Time snapshots are taken at times t_{E1} (1.45 Ga), t_{E2} (4.8 Ga), t_{E3} (5.29 Ga), t_{E4} (5.38 Ga), t_{E5} (5.86 Ga) and t_{E6} (6.49 Ga).